Intrinsic chiral-spin glass and spin glass transitions in compacted Ni_5Al_3/NiO core/shell nanoparticles

P. V. Prakash Madduri[1,2,*] and S. N. Kaul[2,†]

[1]School of Physical Sciences, National Institute of Science Education and Research, HBNI, Jatni-752050, Odisha, India
[2]School of Physics, University of Hyderabad, Central University P.O., Hyderabad-500046, Telangana, India

(Received 13 July 2019; published 24 December 2019)

We report the first synthesis of the intermetallic compound Ni_5Al_3 in the nanocrystalline form. At the nanometer length scale, a stable Ni_5Al_3 compound (core) does not form without a NiO shell. Detailed structural and microstructural characterization as well as the compositional analysis indicate the presence of Ni_5Al_3/NiO core/shell nanoparticles and log-normal crystallite size distribution with mean size $d \simeq 6$ nm. "Zero-field" (dc magnetic field, $H = 0$) linear (χ_1) and nonlinear (χ_n with $n = 2, 3, 4, 5$) ac-magnetic susceptibilities have been measured as functions of temperature at various ac driving field amplitudes over three decades of frequency on the nanocrystalline samples S_1 and S_2 of composition $Ni_{5+x}Al_{3-x}$/NiO ($x = 0.014$) and $Ni_{5-x}Al_{3+x}$/NiO ($x = 0.038$), respectively. $\chi_1(T)$ and $\chi_n(T)$ are shown to provide conclusive evidence for the existence of two spin glass (SG) thermodynamic phase transitions: one at $T_i(H = 0) \simeq 138$ K and the other at a lower temperature $T_p(H = 0) \simeq 108$ K in both S_1 and S_2. Linear ac-susceptibility in superposed dc magnetic fields demonstrates that the thermodynamic nature of these transitions is preserved in finite fields and the H-T phase diagrams for the samples S_1 and S_2 conform very well only with the H-T phase diagram predicted by the chirality-driven spin glass (SG) ordering model for a three-dimensional nearest-neighbor Heisenberg SG system with weak random anisotropy. A detailed comparison between theory and experiment permits us to unambiguously identify various "zero-field" and "in-field" SG phase transitions as (i) the simultaneous paramagnetic (PM): chiral-spin glass (CG) and PM-SG phase transitions at $T_i(H)$ and (ii) the replica symmetry-breaking SG transition at $T_p(H)$.

DOI: 10.1103/PhysRevMaterials.3.126003

I. INTRODUCTION

Transition-metal (TM = Fe, Co, Ni) aluminides (TM_xAl_y) exhibit a rich variety of physical properties due to the dramatic changes in the density of states $N(E_F)$ at the Fermi level E_F caused by the choice of the TM atom, alloy composition (stoichiometric or otherwise), chemical pressure (doping) and local defects (vacancies and antisite disorder) [1,2]. Nickel aluminides (Ni-Al) stand out because a number of stable crystallographic phases have finite homogeneity ranges (i.e., the single phase regions have finite widths) around stoichiometric compositions, spanning Ni concentrations as large as $\simeq$14 *at*. % Ni. Existence of a homogeneity range provides a unique opportunity to study the effects of off-stoichiometry. This is so because the deviations from the stoichiometric composition either result in the substitution of excess nickel atoms onto aluminum sites in the Ni-rich compositions or in the formation of vacancies on the nickel sites in the Al-rich compositions. The crystallographic phase diagram [3] for the Ni-Al binary alloy system asserts that there are five stable equilibrium phases: Ni_3Al, Ni_5Al_3, NiAl, Ni_2Al_3, and $NiAl_3$. Among these phases, Ni_3Al and NiAl [1,3] have attracted maximum attention for the reasons stated below.

The intermetallic compound Ni_3Al has the ordered $L1_2$ (fcc) structure and is, by far, the most extensively studied system [4–6] because it exhibits many fascinating novel physical phenomena, which include: weak itinerant-electron magnetism [4,7–15], pressure-induced [16] or compositional and/or site disorder-induced [17–19] non-Fermi liquid (NFL) behavior in bulk $Ni_{75\pm x}Al_{25\mp x}$, thermoelastic martensitic transformation and ferromagnetic shape memory effects in bulk Fe-doped Ni_3Al [20,21]. In sharp contrast, depending upon the average crystallite size d, nanocrystalline Ni_3Al exhibits exchange-enhanced Pauli spin paramagnetism for $d = 25$ nm [22], antiferromagnetic spin fluctuation-mediated superconductivity and NFL behavior [23] close to the quantum critical point [24] when $d \simeq 50$ nm and chirality-driven intrinsic spin-glass ordering [25] when d ranges from 5 to 50 nm.

By comparison, the equiatomic NiAl phase with an ordered $B2$ (b.c.c) structure is reported to exhibit Pauli paramgnetic behavior [26]. A peculiar minimum in resistivity at $x \simeq 50$ at. % Al in $Ni_{100-x}Al_x$ alloys was observed in the resistivity-x plots [26]. High thermal conductivity, excellent oxidation-resistant property, low-density and high strength, compared to the other Ni-based superalloys, make this compound suitable for aerospace applications such as high-pressure turbine blades [3].

Though the Ni_5Al_3 phase [27–29] is stable at temperatures $\simeq$973 K within the range $\sim$64–68 at. % Ni, and falls in between the NiAl phase (extending from 45 to 59 at. % Ni)

*pavan29587@niser.ac.in
†sn.kaul@uohyd.ac.in

and the Ni_3Al phase (occurring in the range 73–77 at. %Ni) in the Ni-Al phase diagram, hardly anything is known about the physical properties of this Ni-rich intermetallic compound. This is so because it is a formidable task to obtain Ni_5Al_3 as a single phase in the bulk form [29,30]. To elucidate this point further, the formation of the Ni_5Al_3 phase proceeds via a two-step process: the Ni-rich $B2$ NiAl (stable at high temperatures), with excess Ni atoms on Al sites, undergoes Bain distortion [28,31] and transforms into the $L1_0$-NiAl martensite upon quenching from temperatures as high as 1523 K, and the subsequent aging at elevated temperatures (823 K for 15 days) causes ordering of the Ni atoms on the Al sublattice leading to the transformation of the martensite phase into Ni_5Al_3.

In this work, Ni_5Al_3 has been synthesized, for the first time, in the nanocrystalline form, by inert gas condensation (IGC) technique. After a thorough structural, microstructural and compositional characterization, detailed investigation of the magnetic properties of nanocrystalline Ni_5Al_3 has been undertaken with a view to unravel the true nature of the intrinsic magnetic ordering.

II. SYNTHESIS AND CHARACTERIZATION

From several attempts to synthesize the intermetallic compound Ni_5Al_3 in the nanocrystalline state by inert-gas condensation technique [32,33], we found that, at the nanometer length scale, the Ni_5Al_3 compound could be formed only when a target composition richer in the Ni content than the stoitiometric composition is used and the residual oxygen level in the sample chamber is varied by evacuating the chamber to different pressures in the range 10^{-7} to 10^{-8} Torr prior to back-filling the chamber with a few mTorr inert gas (helium) and starting the thermal evaporation process. From this finding, we conclude that a NiO shell is necessary to stabilize the Ni_5Al_3 crystalline core of the nanoparticles. The Ni_5Al_3/NiO core/shell nanoparticles, so synthesized, were compacted *in situ* up to pressures as high as 2 GPa to form discs (referred to as the samples S_1 and S_2) of 8 mm diameter and 0.355 mm thickness. Rietveld analysis of room temperature x-ray diffraction (XRD) patterns, taken on S_1 and S_2, revealed that a major Ni_5Al_3 phase coexists with a minor NiO phase, as is evident from Fig. 1.

Ni_5Al_3 compound has the Pt_5Ga_3-type orthorhombic unit cell structure with space group D_{2h}^{19} ($Cmmm$) [27,28], whereas NiO belongs to the Fm-$3m$ (face-centered cubic) space group. Numerical estimates of the phase fractions, lattice parameters and lattice strains of the individual phases are given in Table I. Significant broadening of the diffraction peaks indicates that the samples under investigation are made up of tiny crystallites in the sub-micron range. From the XRD data, the volume-weighted mean crystallite size (d) has been determined as follows. The linewidth β_{hkl} of a Bragg peak of given (hkl), obtained from the Rietveld refinement of the XRD pattern, is the sum of size- (β_d) and strain-broadening (β_ε) contributions. The size-strain plots [35], shown in the sub-Figs. 1(c) and 1(d), are based on the relation $(\beta^*_{hkl}/d^*_{hkl})^2 = (1/d)\,(\beta^*_{hkl}/(d^*_{hkl})^2) + (\varepsilon/2)^2$, where $\beta^*_{hkl} = \beta_{hkl}\,cos\theta/\lambda$ and $d^*_{hkl} = 2d_{hkl}\sin\theta/\lambda$ and ε is the strain, yielded by the Halder-Wagner approximation [36]. Thus, intercept (on the ordinate) and slope of the linear $(\beta^*_{hkl}/d^*_{hkl})^2$ versus $(\beta^*_{hkl}/(d^*_{hkl})^2)$ plot

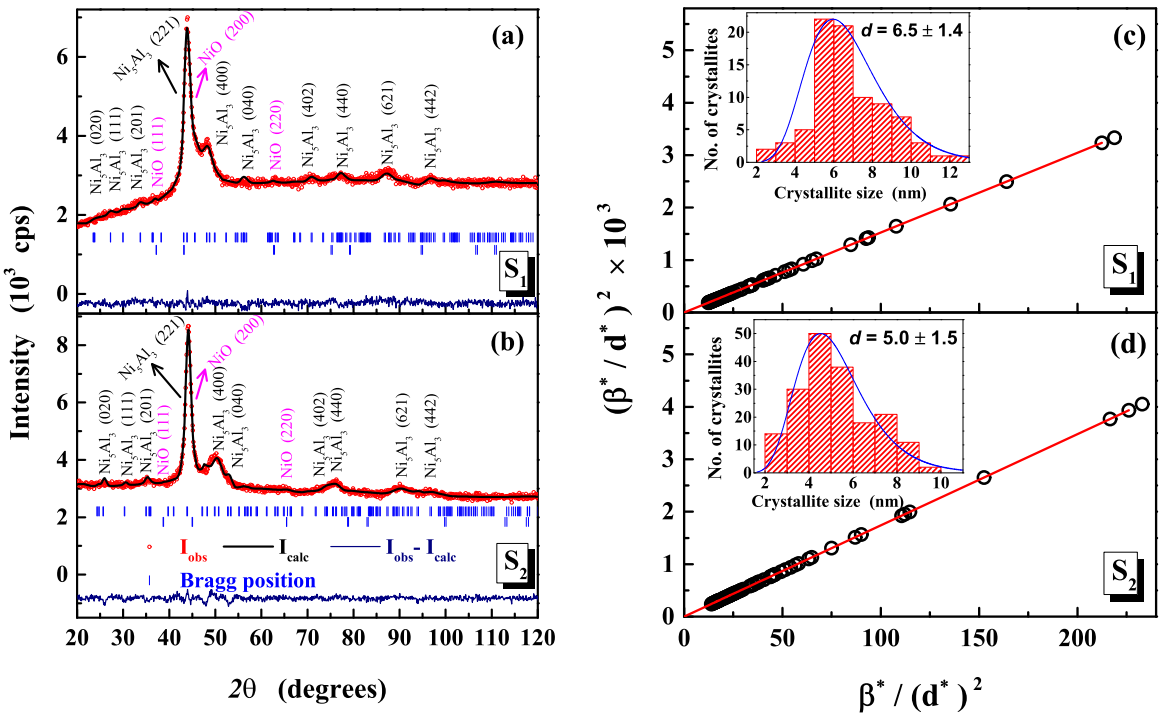

FIG. 1. [(a) and (b)] Room-temperature x-ray diffraction patterns along with the Rietveld refinement fits for the samples S_1 and S_2. Note that, for the sake of clarity, the Miller indices are shown only for the prominent Bragg peaks. The linear Halder-Wagner plots, shown in the right panels (c) and (d), and based on the relation [36] $(\beta^*_{hkl}/d^*_{hkl})^2 = (1/d)\,(\beta^*_{hkl}/(d^*_{hkl})^2) + (\varepsilon/2)^2$ (for definitions of the symbols, see text), yield the average crystallite size d as 6 ± 1 nm for both S_1 and S_2. Insets of (c) and (d) highlight the log-normal distribution of crystallite sizes (obtained from the TEM images) in both the samples.

TABLE I. Structural information from Rietveld refinement of the XRD patterns; for details, refer to Table S1 [34].

Samples	Phases	Phase fractions (%)	lattice parameters (Å)	lattice strain
S_1	Ni_5Al_3[a]	84.0(2.0)	$a = 7.580(4), b = 6.561(4), c = 3.734(2)$	6.4×10^{-4}
	NiO[a]	16.0(1.0)	$a = b = c = 4.185(3)$	–
S_2	Ni_5Al_3[a]	79.4(2.7)	$a = 7.211(4), b = 7.059(4), c = 3.658(2)$	2.1×10^{-3}
	NiO[a]	20.6(1.1)	$a = b = c = 4.120(2)$	–
	Bulk-Ni_5Al_3[b]	100	$a = 7.475, b = 6.727, c = 3.732$	–
	Bulk-NiO[c]	100	$a = b = c = 4.170(2)$	–

[a]Present work.
[b]ICDD-04-007-0381.
[c]ICDD-04-002-5335.

determine the average strain ε and average crystallite size d, respectively. The values of d, so determined, for the samples S_1 and S_2 are 6.5 ± 1.0 and 5.0 ± 1.5 nm. Compositional analysis of the samples by wavelength dispersion x-ray spectroscopy (WDS) yielded the composition of the samples as, $S_1 : 84.98\%Ni_{5+x}Al_{3-x}$ $(x = 0.0144) + 15.02\%$ NiO and $S_2 : 79.80\ \%\ Ni_{5-x}Al_{3+x}$ $(x = 0.0384) + 20.20\%$ NiO. The phase fractions estimated from the detailed WDS analysis are in excellent agreement with those obtained from the Rietveld refinement of the XRD patterns (see Table I). The microstructure and crystallite size distribution were determined by high-resolution transmission electron microscopy (HR-TEM). Since the samples are brittle in nature, they could be powdered using a mortar and pestle. The powder was dispersed in ethanol by ultrasonic shaker. The dispersion was drop-cast onto a copper grid and dried, before the TEM examination. TEM images of agglomerates and individual crystallites as well as the selected-area electron diffraction (SAED) patterns, are shown in Fig. 2. TEM images in Fig. 2 indicate that Ni_5Al_3 crystalline core of average size $\simeq 6$ nm is surrounded by a structurally disordered NiO shell; the latter inference is drawn from the absence of lattice fringes corresponding to the shell. Disordered nature of the NiO shell is also supported by the unusually broad x-ray Bragg peaks of the NiO phase [Figs. 1(a) and 1(b)] and the diffuse rings in the SAED pictures (Fig. 2). Note that these rings and the bright spots on them correspond to the Bragg reflections of NiO and Ni_5Al_3, respectively. Furthermore, the spacing between the lattice fringes observed for the Ni_5Al_3 core corresponds to the set of parallel (221) atomic planes.

A large number of crystallites of different sizes were visually counted from the TEM images taken from different regions of the sample and their sizes were determined by the ImageJ software package. The crystallite size histograms are displayed in the insets of Figs. 1(c) and 1(d). The size distribution is well represented by the log-normal distribution with a mean crystallite size (d) of 6.5(1.4) nm for S_1 and 5.0(1.5) nm for S_2. The numbers in the parentheses give the standard deviation in d. These values of d compare favorably with those determined from the Halder-Wagner plots [Figs. 1(c) and 1(d)].

III. AC MAGNETIC RESPONSE

The first five harmonics of the ac magnetic response comprising the real and imaginary components of *linear* (χ_1) as well as second to fifth-order *nonlinear* magnetic susceptibilities (χ_2–χ_5) of the nanocrystalline Ni_5Al_3/NiO samples, S_1 and S_2, were measured over the temperature range 1.8–320 K at the rms amplitudes $h_{ac} = 0.1$, 1 and 10 Oe and frequencies $11\ \text{Hz} \leqslant \omega \leqslant 9999$ Hz of the ac driving field, using Quantum Design PPMS-ACMS option. $\chi_1(T)$ was also measured at $h_{ac} = 1$ Oe and $\omega = 111$ Hz in fixed superposed dc fields, $H \equiv H_{dc}$, in the range 0–100 Oe. All the measurements were

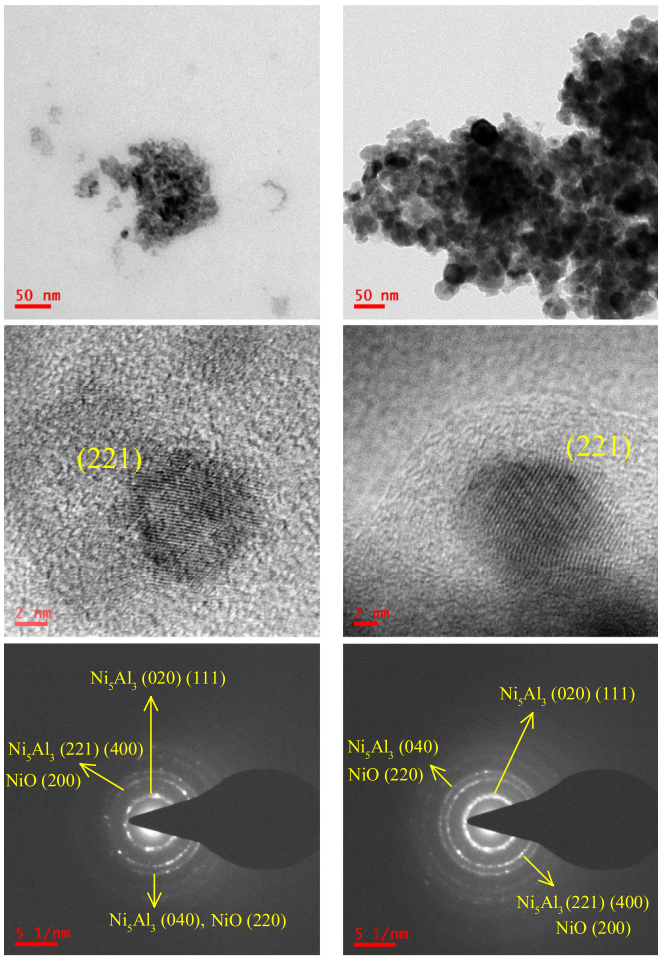

FIG. 2. Transmission electron microscope (TEM) images of the nanoparticle agglomerates, high-resolution TEM images of single nanoparticles, and selected area electron diffraction (SAED) patterns of the samples S_1 (left panels) and S_2 (right panels).

carried out on the discs of 3 mm diameter spark-cut from the 8-mm diameter nanocrystalline Ni_5Al_3/NiO discs, prepared by inert gas condensation.

The nonlinear magnetic susceptibilities, defined by the expansion of the magnetization m in powers of a weak external magnetic field $h = h_{ac} + h_{dc}$, as

$$m = m_0 + \chi_1 h + \chi_2 h^2 + \chi_3 h^3 + \chi_4 h^4 + \chi_5 h^5 + \ldots \quad (1)$$

[where m_0 is the spontaneous magnetization, χ_1 is the linear susceptibility and χ_n ($n = 2, 3,...$) are the nonlinear susceptibilities] were measured because they enable an unambiguous distinction to be made between different types of magnetic order. To briefly illustrate this point, the above relation with $m_0 \neq 0$ describes ferromagnetic order at $T < T_C$, as opposed to the paramagnetic state at $T > T_C$ or a spin glass (SG) state at all temperatures (including the critical region near the SG transition temperature) when $m_0 = \chi_2 = \chi_4 = 0$.

IV. LINEAR SUSCEPTIBILITY

A. Frequency dependence

Figure 3 displays the temperature variations of the linear ac magnetic susceptibility (χ_1) for the samples S_1 and S_2 at fixed frequencies ranging from 11 to 9999 Hz in the temperature range 2 K $\leqslant T \leqslant$ 200 K without superposed dc field. The main observations are as follows. In both the samples S_1 and S_2, $\chi_1(T)$ exhibits a peak at $T_p \simeq 108$ K (where $d\chi_1/dT = 0$) and an inflection point at $T_i \simeq 138$ K [where $d\chi_1(T)/dT$ goes through a *sharp minimum*]. That T_p and T_i mark the temperatures at which two different types of spin glass transitions occur and the exact nature of these transitions will become clear in the subsequent text. For a given frequency, these characteristic temperatures remain essentially unaltered when h_{ac} increases from 0.1 to 1.0 Oe, but change drastically at $h_{ac} = 10$ Oe. At any given h_{ac} in both S_1 and S_2, T_p and T_i get displaced to higher temperatures with increasing frequency and the values of χ_1 at these temperatures decrease, as is normally the case with spin glasses or superparamagnets.

Since the Curie temperature T_c, at which a thermodynamic phase transition from a ferromagnetic (FM) state to a paramagnetic (PM) state occurs, does not depend on the choice of the experimental time-window, the dependence of T_p and T_i on frequency completely rules out the possibility of a FM-PM phase transition at these temperatures. A standard measure of the frequency-induced peak-shift that facilitates a direct comparison between different spin glass (SG) and/or superparamagnet (SP) systems is the fractional change in T^* (in the present case, T^* stands for T_p or T_i) per decade of frequency, $\triangle T^*/(T^* \triangle \log_{10}\omega)$; $T^*(\omega) \longrightarrow T_g$ in the limit $\omega \longrightarrow 0$ while T_g denotes the transition temperature for a SG or the blocking temperature for a SP. The values of the quantities $\triangle T_p/(T_p \triangle \log_{10}\omega)$ and $\triangle T_i/(T_i \triangle \log_{10}\omega)$, determined in this work for S_1 and S_2 at $h_{ac} = 0.1$, 1, and 10 Oe, are listed in Table II. These values are closer to the peak-shift per decade of frequency, previously reported in the chirality-driven spin glass system Ni_3Al nanoparticle aggregates [25] and for the canonical spin glasses (AgMn, CuMn, AuMn, PdMn) [37–39]. This agreement strongly indicates that the nanocrystalline systems in question could be spin glasses.

In order to verify whether or not the observed magnetic ordering conforms to that of a spin glass, we follow the customary approach to ascertain if the frequency-induced shift in T_p and T_i can be explained in terms of the critical slowing down (CSD) model [40–42] for a spin glass. This model

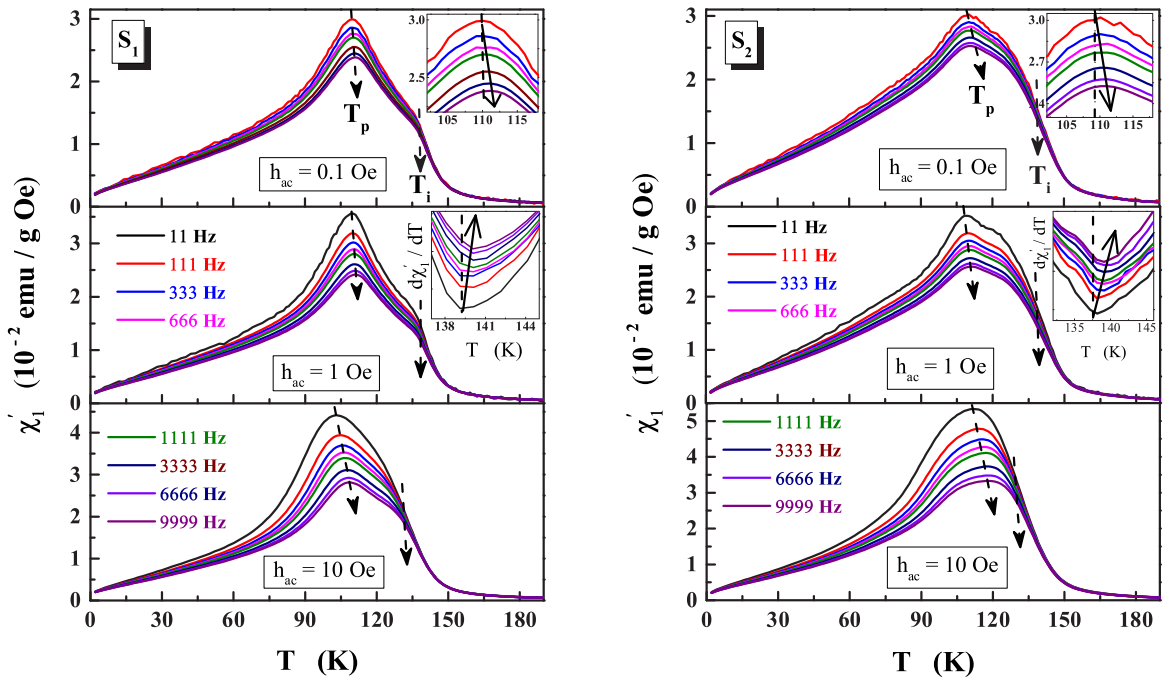

FIG. 3. Linear susceptibility, $\chi_1'(T)$, for the nanocrystalline samples S_1 and S_2 in the temperature range 2 K $\leqslant T \leqslant$ 200 K at the rms amplitudes of the ac driving field $h_{ac} = 0.1$, 1, and 10 Oe and frequencies, ω, ranging from 11 to 9999 Hz. Insets highlight the small but finite shift of T_p [the temperature at which $\chi_1'(T)$ peaks] and T_i [where $d\chi_1'(T)/dT$ goes through a minimum] to higher temperatures with increasing frequency. The vertical dashed line, marking the T_p or T_i for the lowest frequency, serves as a reference for the frequency-induced shift.

TABLE II. Relative shift in the transition temperatures T_p and T_i per decade of frequency.

Sample	h_{ac} (Oe)	$\Delta T_p/[T_p\,\Delta \log_{10}\omega]$	$\Delta T_i/[T_i\,\Delta \log_{10}\omega]$
S_1[a]	0.1	0.0050(2)	0.0053(3)
	1.0	0.0055(2)	0.0043(3)
	10.0	0.0124(5)	0.0182(5)
S_2[a]	0.1	0.0053(3)	0.0046(3)
	1.0	0.0071(3)	0.0042(2)
	10.0	0.0113(2)	0.0038(3)
nc-Ni_3Al[b]	1.0	0.0055(1)	0.0022(2)
CuMn[c]	0.1	0.0050	–
AuMn[d]	0.1	0.0045	–
AgMn[e]	0.1	0.0060	–

[a]Present work.
[b]Reference [25].
[c]Reference [37].
[d]Reference [38].
[e]Reference [39].

predicts the following functional dependence of T^* on ω:

$$\omega = \omega_0 \left[\frac{T^*(\omega) - T_g}{T_g}\right]^{z\nu}, \tag{2}$$

where ω_0 is the attempt frequency, $T_g = T^*(\omega = 0)$ is the true spin glass freezing temperature, z is the dynamic critical exponent that characterizes the relaxation rate of the correlated spin-cluster dynamics (the critical slowing down) and ν is the critical exponent for the spin-spin correlation length. The *linear* $\log_{10}(\omega/\omega_0)$ versus $\log_{10}([T^*(\omega) - T_g]/T_g)$ plots in Fig. 4 testify to the validity of the CSD model with the choice of the parameters (Table III) that are typical of canonical spin glasses CuMn, PtMn, etc. For conventional spin glass systems, ω_0 is $\sim 10^9$–10^{13} and $z\nu$ lies in the range 4–10. The presently determined values for the quantity $z\nu$ are in excellent agreement with those ($z\nu = 5.0(5)$ [43] and $z\nu = 5.5(1)$ [44–48]), predicted by the three-dimensional Heisenberg chiral spin glass model which considers nearest-neighbor exchange interactions with Gaussian distribution.

TABLE III. Critical slowing down model parameters. SG(i) and SG(p) stand for the spin glass (SG) transitions occurring at frequency-dependent temperatures T_i and T_p, respectively.

Sample	h_{ac} (Oe)	Transition	ω_0 (Hz)	$z\nu$	T_g (K)
S_1	0.1	SG(p)	$1.12(15) \times 10^{12}$	5.4(4)	108.45(50)
	0.1	SG(i)	$3.42(38) \times 10^{12}$	5.5(5)	138.50(50)
	1.0	SG(p)	$8.26(6) \times 10^{11}$	5.1(1)	108.74(60)
	1.0	SG(i)	$2.50(7) \times 10^{12}$	5.1(3)	138.63(50)
	10.0	SG(p)	$3.30(60) \times 10^{10}$	5.3(4)	102.00(50)
	10.0	SG(i)	$5.20(20) \times 10^{10}$	5.5(5)	129.60(20)
S_2	0.1	SG(p)	$7.52(90) \times 10^{11}$	5.0(1)	108.36(50)
	0.1	SG(i)	$2.39(40) \times 10^{12}$	5.0(2)	138.34(50)
	1.0	SG(p)	$1.44(60) \times 10^{12}$	5.6(2)	108.56(50)
	1.0	SG(i)	$2.18(70) \times 10^{12}$	4.99(4)	138.75(50)
	10.0	SG(p)	$9.60(20) \times 10^{9}$	5.0(2)	111.50(50)
	10.0	SG(i)	$5.00(10) \times 10^{11}$	4.5(5)	131.50(50)

The data presented in Fig. 3 assert that both samples S_1 and S_2 exhibit two SG-like transitions each: one at $T_g \equiv T_i(\omega = 0)$ and the other at $T_g \equiv T_p(\omega = 0)$. The T_g values at different h_{ac} are given in Table III.

B. Direct-current field dependence

In order to find out whether or not the "zero-field" SG transitions are affected by finite static magnetic fields, the

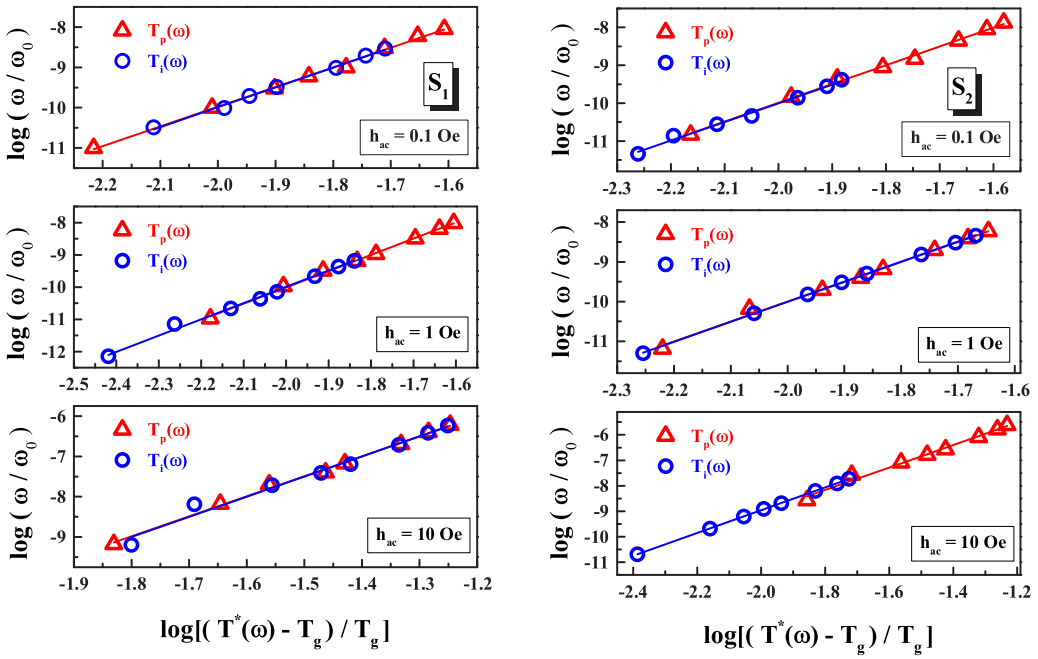

FIG. 4. The linear $\log_{10}(\omega/\omega_0)$ vs $\log_{10}([T^*(\omega)\text{-}T_g]/T_g)$ plots with $T^*(\omega)$ standing for either $T_p(\omega)$ or $T_i(\omega)$ and $T_g = T^*(\omega = 0)$, validate the critical slowing down model [40–42], proposed for a spin glass, in the samples S_1 (left) and S_2 (right).

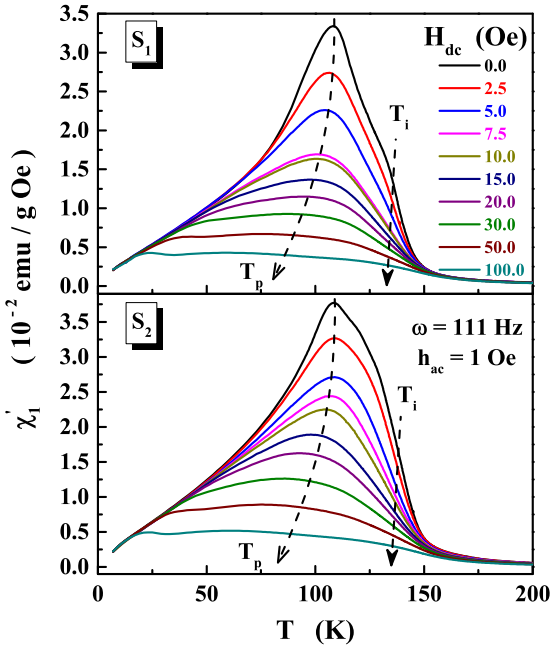

FIG. 5. Temperature variations of the "in-phase" component of ac susceptibility, χ_1', at $h_{ac} = 1$ Oe and frequency, $\omega = 111$ Hz, measured in the superposed dc magnetic fields, on the samples S_1 and S_2, over the temperature range 2 K $\leqslant T \leqslant$ 200 K.

"in-phase" (χ_1') and "out-of-phase" (χ_1'') components of linear ac susceptibility were measured at $h_{ac} = 1$ Oe and $\omega =$ 111 Hz in different superposed dc magnetic fields $H \equiv H_{dc}$.

TABLE IV. Parameters for the fits based on Eq. (3).

Parameters	S_1	S_2
Field range (Oe)	$0 \leqslant H \leqslant 30$	$0 \leqslant H \leqslant 30$
$T_p(0)$ (K)	108.92(25)	108.94(26)
C_p (Oe^{-n_p})	0.0188(3)	0.0195(3)
n_p	0.67(1)	0.67(2)
$T_i(0)$ (K)	138.40(50)	138.00(30)
C_i (Oe^{-n_i})	0.0097(2)	0.0072(1)
n_i	0.67(1)	0.67(2)

As is evident from Fig. 5, in both samples, the peak in $\chi_1'(T)$ (also in $\chi_1''(T)$ but not shown) gets progressively suppressed, smeared out and displaced to lower temperatures with increasing H_{dc}. H_{dc} shifts the inflection point (and hence T_i) also to lower temperatures but at a slower rate than in the case of T_p. Figure 6 shows that the temperatures $T_p(H)$ [at which $\chi_1'(T)$ peaks] and $T_i(H)$ [which corresponds to the inflection point in $\chi_1'(T)$ at fixed H] vary with the static field in accordance with the relation

$$t_x = \frac{T_x(0) - T_x(H)}{T_x(0)} = C_x \; H^{n_x}, \tag{3}$$

where the subscript x in Eq. (3) stands for either p or i and the parameters $T_x(0)$, C_x and n_x are given in Table IV. The $T_x(H)$ data, shown in Fig. 6, are re-plotted in the form of the H-T diagram in Fig. 7(a) to facilitate a direct comparison of $T_x(H)$ with theoretical predictions. There are basically two types of theoretical models [25,49]: (I) the mean-field

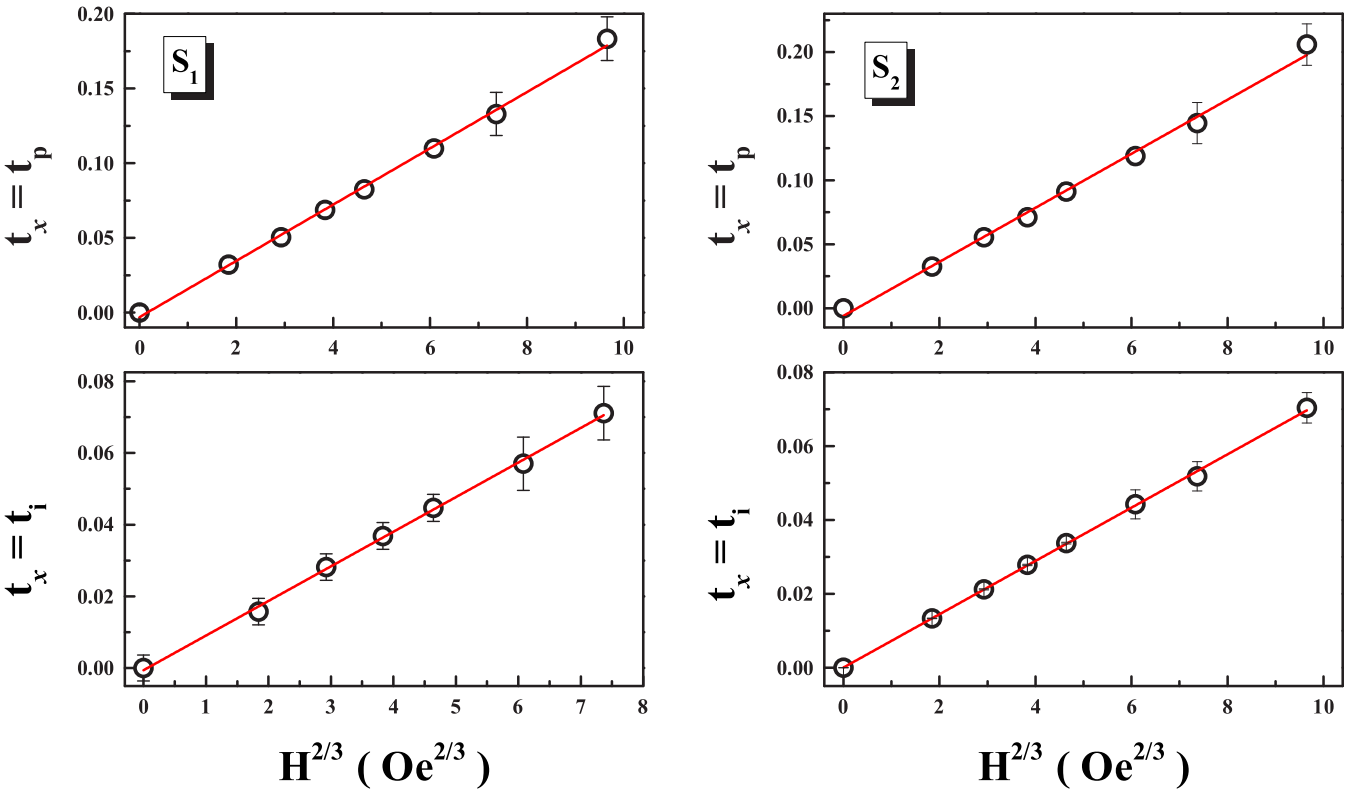

FIG. 6. $H^{2/3}$ power-law variations of the reduced field-induced shifts (t_p and t_i) in the critical temperatures T_p and T_i.

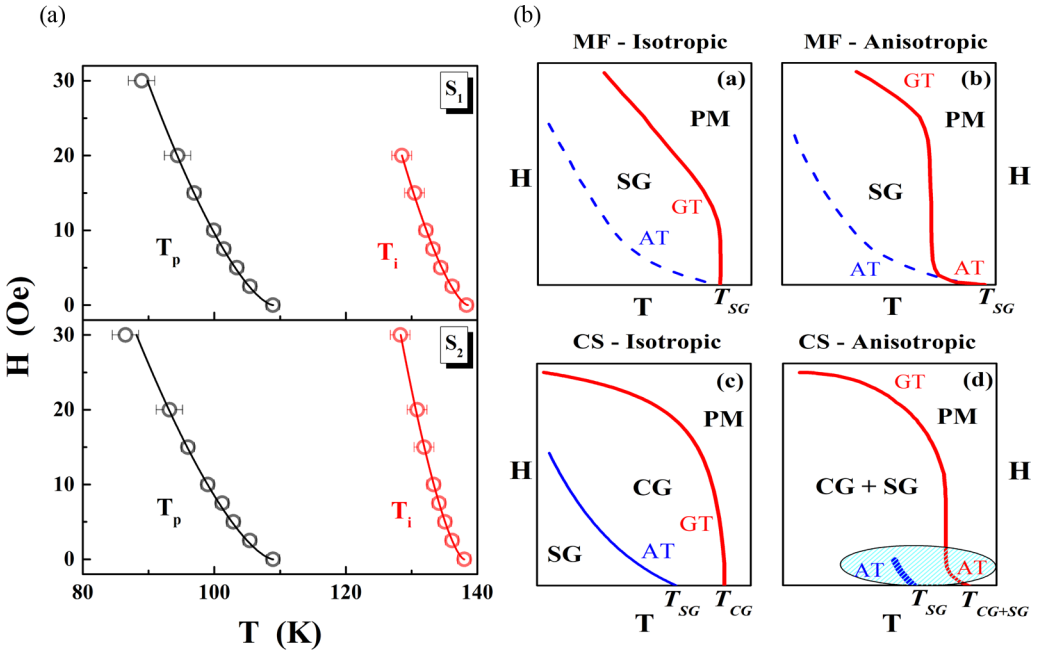

FIG. 7. (a) H-T phase diagrams for the samples S_1 and S_2. (b) Schematic sketches of the $H-T$ phase diagrams predicted by the mean-field (MF) and chiral-spin (CS) models for the isotropic and anisotropic cases, as elucidated in the text. The notations SG, CG, and PM refer to spin glass, chiral glass, and paramagnetic phases. AT and GT refer to the literature (see text).

(MF) models [49–51] for a three-dimensional (3D) isotropic Heisenberg vector-spin glass with [49,52] or without [50] weak random anisotropy (RA), in which the spin components interact with one another through infinite-range exchange interactions, and (II) the chiral-spin (CS) models [25,44–48,53] for an isotropic classical 3D Heisenberg spin glass system in which the spin-frustration-induced, energetically degenerate 'left-handed' and 'right-handed' chiral states of local noncoplanar spin structures coexist with spins coupled by nearest-neighbor exchange interactions. Like the MF models, the chiral-spin models deal with both the isotropic and weak RA cases. The MF models for a 3D Heisenberg spin glass with or without weak RA predict only one "zero-field" SG transition at $T_g(0)$ which, in the isotropic case, branches out into the Gabay-Toulouse (GT) [50] and Almeida-Thouless (AT) [51] irreversibility lines in finite fields. RA does not affect the AT line but converts the GT line into the AT transition line at weak fields which crosses over to the GT line at higher fields [52]. The GT (AT) irreversibility line is given by Eq. (3) with the subscript x replaced by GT (AT) and $n_{\rm GT} = 2$ ($n_{\rm AT} = 2/3$). In the isotropic case, the chiral-spin models predict that, when a 3D isotropic Heisenberg spin glass system is cooled in zero field, the system undergoes a chiral-glass (CG) transition at a finite temperature $T = T_{\rm CG}(0)$ followed by a spin-glass (SG) transition at a lower temperature $T = T_{\rm SG}(0) < T = T_{\rm CG}(0)$. In finite fields, the CG and SG transition lines, $T_{\rm CG}(H)$ and $T_{\rm SG}(H)$, have the same functional form *at low fields* as that of the GT and AT lines. In the presence of weak RA, the chiral-spin models for a 3D Heisenberg spin glass system make the following predictions. When $H = 0$, the CG and SG transitions occur *simultaneously* at a finite temperature $T_{\rm CG+SG}(0)$, followed by another SG transition at a lower temperature $T_{\rm SG}(0) < T_{\rm CG+SG}(0)$. At sufficiently low fields (where RA dominates over H), the $T_{\rm CG+SG}(H)$ and $T_{\rm SG}(H)$ phase transition lines have the AT form. By contrast, at sufficiently high fields (where H swamps RA), the $T_{\rm CG+SG}(H)$ transition line has the GT form.

Schematic sketches of the H-T diagrams for the 3D Heisenberg spin glass without (isotropic case) and with weak random anisotropy (anisotropic case), predicted by the mean-field (MF: type I) and the chiral-spin (CS: type II) models, are shown in the panels (a) and (b) for MF and (c) and (d) for CS in Fig. 7(b). The observed H-T diagrams [displayed in Fig. 7(a)], when compared with those yielded by the models of type I and type II [sketched in Fig. 7(b)], completely rule out the applicability of the MF models to the present case since they predict only one zero-field SG transition as against two $H = 0$ SG transitions observed in this work. Such a comparison also brings out clearly that the H-T diagrams for both the samples S_1 and S_2 conform well with only the weak random anisotropy case [i.e., with the shaded portion of the H-T diagram in the panel (d) of Fig. 7(b)] within the chirality-driven SG ordering scenario. Thus, the phase transition lines $T_i(H)$ and $T_p(H)$, of the AT form at low fields, can be unambiguously identified with $T_{\rm CG+SG}(H)$ and $T_{\rm SG}(H)$, respectively. Note that $T_{\rm CG+SG}(H)$ is the temperature at any given H (including $H = 0$) at which the paramagnetic (PM) to chiral-spin glass (CG) and the PM-SG phase transitions occur *simultaneously*, whereas $T_{\rm SG}(H)$ is the field-dependent temperature at which the CG + SG mixed phase transforms to the replica symmetry-breaking SG phase.

V. NONLINEAR SUSCEPTIBILITIES

Figures 8 and 9 depict the temperature variations of the odd harmonics (χ_1, $\chi_3\, h_{\rm ac}^2$, $\chi_5\, h_{\rm ac}^4$) and even harmonics ($\chi_2\, h_{\rm ac}$, $\chi_4\, h_{\rm ac}^3$) of the ac magnetic response observed in the samples S_1 and S_2 over the temperature ranges 1.8–200 K at the ac driving

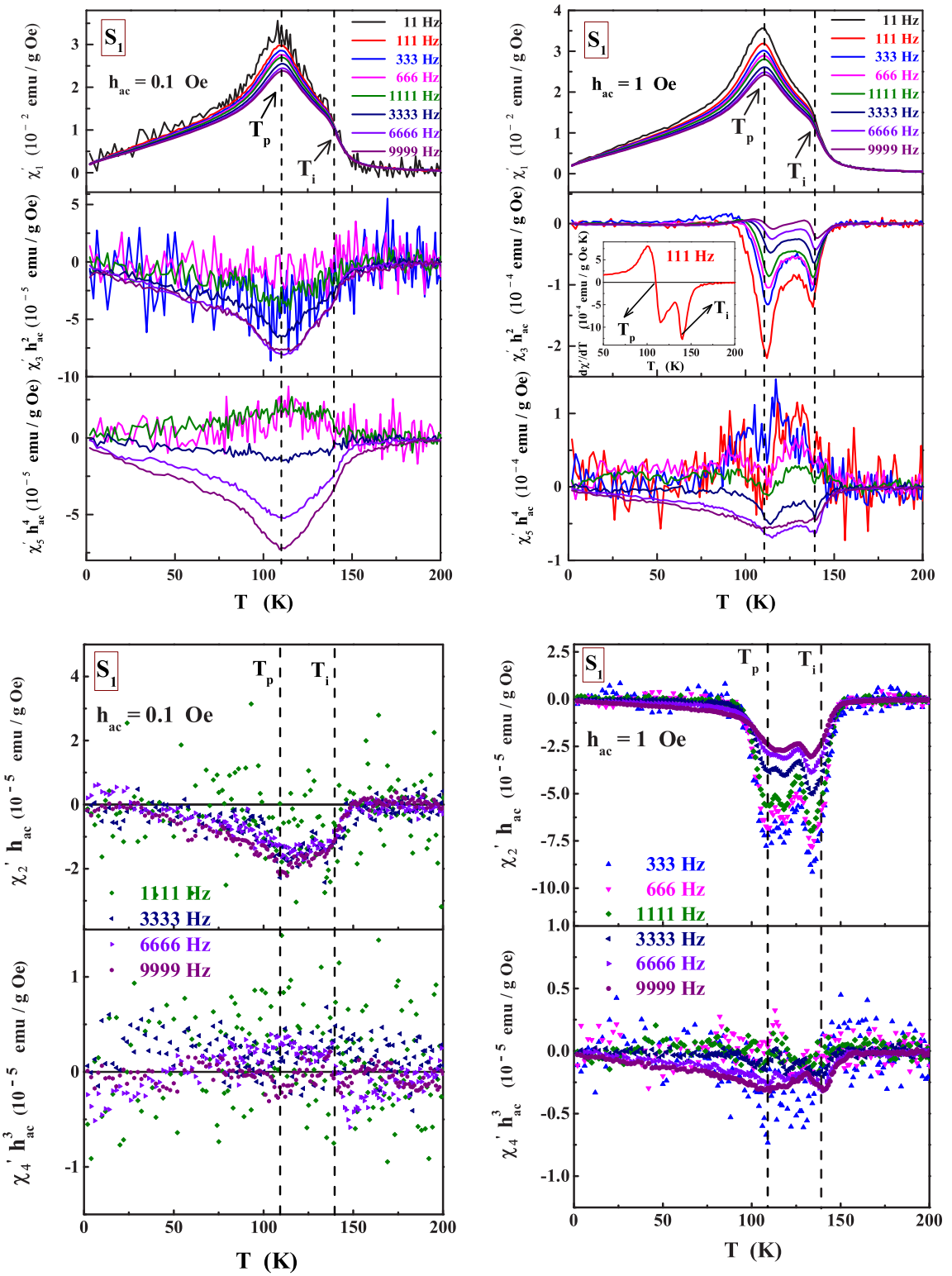

FIG. 8. Odd harmonics, χ_1, $\chi_3\, h_{ac}^2$, and $\chi_5\, h_{ac}^4$ (top) and even harmonics, $\chi_2\, h_{ac}$ and $\chi_4\, h_{ac}^3$ (bottom) of the ac magnetic response as functions of temperature in the range 2 K $\leqslant T \leqslant$ 200 K at $h_{ac} = 0.1$ Oe, 1 Oe and frequencies, ω, ranging from 11 to 9999 Hz for S_1. The inset depicts that, as a function of temperature, the temperature derivative of $\chi_1(T)$, $d\chi_1/dT$, at $\omega = 111$ Hz and $h_{ac} = 1$ Oe goes through a *sharp minimum* at T_i and *changes sign* at T_p. The same features in $d\chi_1/dT$ are observed at other values of ω and h_{ac} as well.

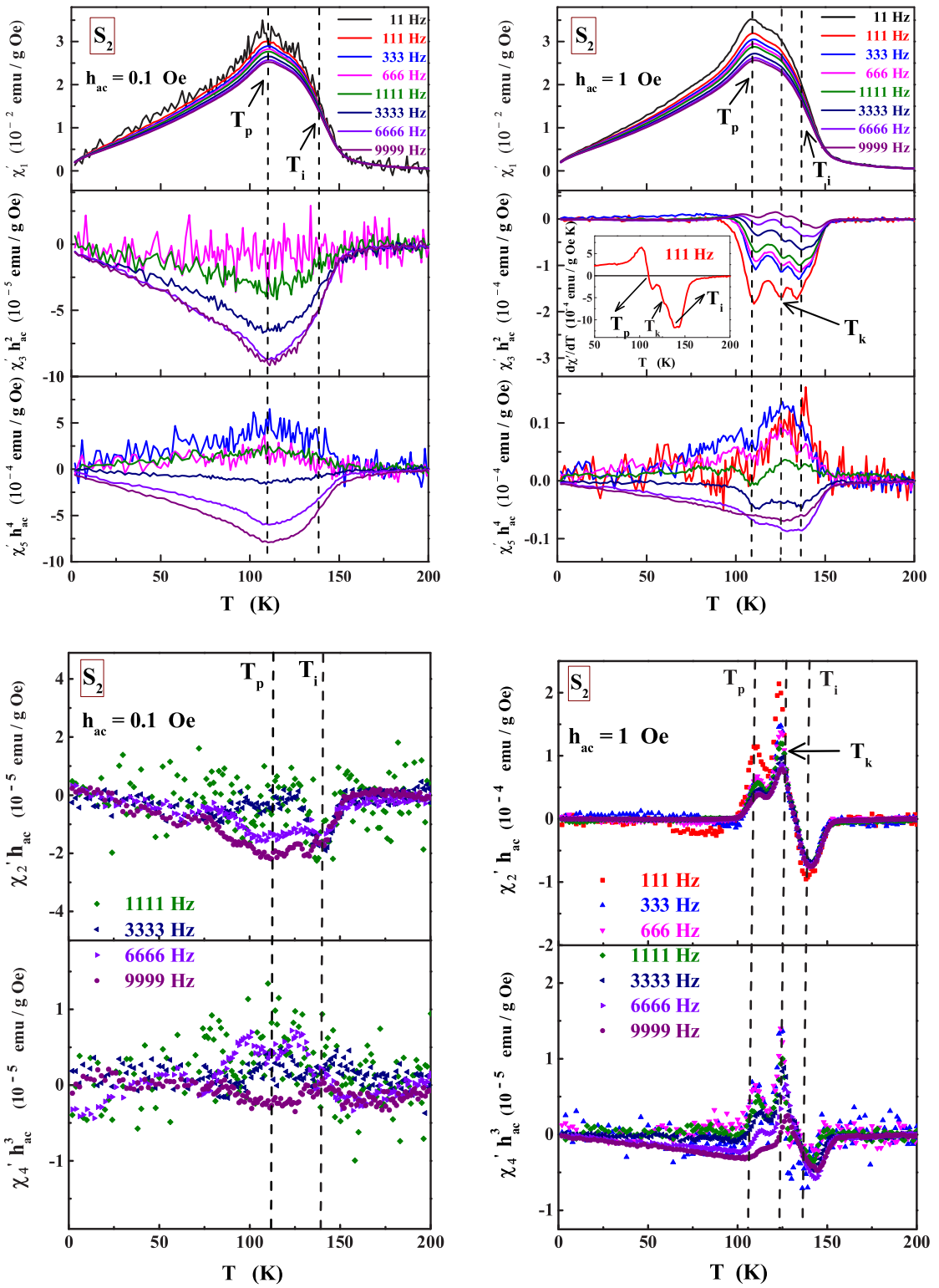

FIG. 9. Odd harmonics, χ_1, $\chi_3\, h_{\rm ac}^2$, and $\chi_5\, h_{\rm ac}^4$ (top) and even harmonics, $\chi_2\, h_{\rm ac}$ and $\chi_4\, h_{\rm ac}^3$, (bottom) of the ac magnetic response as functions of temperature in the range 2 K $\leqslant T \leqslant$ 200 K at $h_{\rm ac} = 0.1$ and 1 Oe and frequencies, ω, ranging from 11 to 9999 Hz for S_2. The inset depicts that, as a function of temperature, the temperature derivative of $\chi_1(T)$, $d\chi_1/dT$, at $\omega = 111$ Hz and $h_{\rm ac} = 1$ Oe goes through a *sharp minimum* at T_i and *changes sign* at T_p. The same features in $d\chi_1/dT$ are observed at other values of ω and $h_{\rm ac}$ as well.

field amplitudes $h_{ac} = 0.1$ Oe and 1 Oe, and frequencies in the range 11 Hz $\leqslant \omega \leqslant$ 9999 Hz. The insets of Figs. 8 and 9 serve to illustrate how the temperatures corresponding to the inflection point ($T_i \equiv T_{CG+SG}$) and the peak ($T_p \equiv T_{SG}$) in $\chi_1(T)$ are accurately determined by the temperatures where the temperature derivative of $\chi_1(T)$, $d\chi_1/dT$, goes through a *sharp minimum* and *changes sign*. It is evident from Figs. 8 and 9 that, contrasted with the very noisy signals for all the harmonics (odd and even) at $h_{ac} = 0.1$ Oe, particularly at low frequencies, the linear and nonlinear susceptibility data taken at $h_{ac} = 1$ Oe exhibit well-resolved features at most frequencies. This is so because, barring the first harmonics, the higher harmonics signals at $h_{ac} = 0.1$ Oe for all ω are weaker by an order of magnitude than those at $h_{ac} = 1$ Oe. The higher the order of harmonics, the weaker the signal, with the result that it approaches the instrumental resolution limit at $\omega < 3333$ Hz. Thus, the data taken at $h_{ac} = 1$ Oe are better suited for a meaningful comparison with theoretical predictions. To facilitate such a comparison, rough sketches of the characteristic experimental signatures in $\chi_1(T)$, $\chi_3(T)$, $\chi_5(T)$ and $\chi_2(T)$, $\chi_4(T)$ in the critical region near FM-PM and SG-PM transitions, predicted by the theory [54–57] for an *ideal* ferromagnet (FM) and spin glass (SG), are shown in Fig. 10. A direct one-to-one comparison between the experimentally observed (Figs. 8 and 9) and theoretically predicted (Fig. 10) temperature variations and the signs of the odd and even harmonics reveals the following. The well-defined *negative cusps* at T_p and T_i at all frequencies in $\chi_3(T)$ and for $\omega \gtrsim 1111$ Hz in $\chi_5(T)$, when $h_{ac} = 1$ Oe, and the shift to higher temperatures of T_p and T_i with increasing ω (clearly visible in Figs. 8 and 9) provide strong evidence for the two SG transitions in both the samples S_1 and S_2. Note that in S_2, an additional minimum at the temperature, $T_k \simeq 125$ K, at which a 'knee' appears in $\chi_1(T)$, is observed at all ω in $\chi_3(T)$. However, in sharp contradiction with the theoretical prediction that, for an *ideal* spin glass, $\chi_2 = \chi_4 = 0$ at all temperatures, including those embracing the critical region near T_g, two negative-minima at the *frequency-dependent* T_p and T_i (positive peaks at T_p and T_k, and a negative minimum at T_i) are observed in $\chi_2(T)$ at all frequencies and in $\chi_4(T)$ for $\omega \gtrsim 1111$ Hz in the sample S_1 (S_2). From the theoretical standpoint, a negative divergence at $T = T_C$ in $\chi_2(T)$ and $\chi_4(T)$ is symptomatic of a conventional FM-PM phase transition (Fig. 10). The frequency dependence of the temperatures at which such minima/peaks occur completely rule out thermodynamic FM-PM phase transitions. Moreover, the occurrence of two successive FM-PM transitions in S_1 is incomprehensible: if the transition at T_p is a FM-PM transition, the transition at a higher temperature T_i cannot be a yet another FM-PM transition. The reverse is also true. We believe that the minima and/or peaks in $\chi_2(T)$ and $\chi_4(T)$ mark strong departures from ideal SG behavior and their origin lies in the frustration-driven chiral-spin structures (rather than the frustrated individual spins) prevalent in the Ni_5Al_3 nanoparticle cores. Such spin structures interact with one another through the competing exchange interactions generated in the intervening structurally-disordered NiO shells having noncollinear antiferromagnetic order.

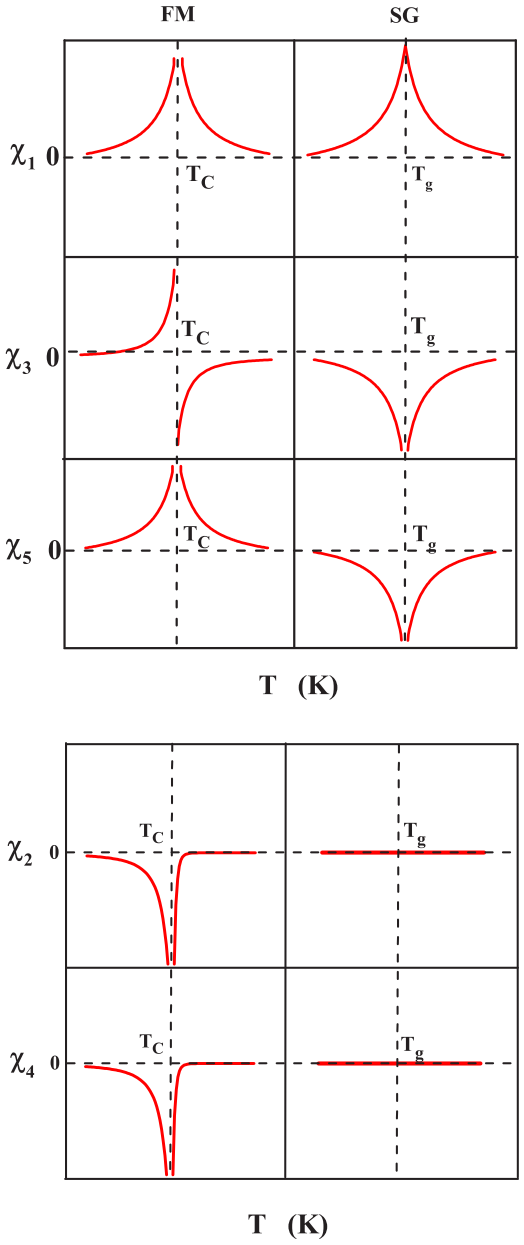

FIG. 10. Schematic depiction of the temperature variations of the odd harmonics (χ_1, χ_3 and χ_5) and even harmonics (χ_2 and χ_4) of the ac magnetic response at the reduced field $h = 1$, predicted by theory [54–58] for a ferromagnet (FM) and a spin glass (SG) in the critical region.

At this stage, it should be emphasized that the global nature of spin glass ordering emerges only in the limit $\omega \to 0$ and $h_{ac} \to 0$. That this is indeed the case in the samples S_1 and S_2, is borne out by the observation that $\chi_2 = \chi_4 \to 0$ (indicated by very weak resolution-limited signals and the statistically scattered data around "zero") at $h_{ac} = 0.1$ Oe as the ac driving-field frequency falls below 1111 Hz.

Thus a thorough discussion of the zero-field/in-field linear ac-magnetic susceptibility, $\chi_1(T, H)$ and nonlinear susceptibilities $\chi_2(T)$, $\chi_3(T)$, $\chi_4(T)$ and $\chi_5(T)$ enables us to conclude that the Ni_5Al_3/NiO core/shell nanoparticle samples, S_1 and

S_2, behave as a 3D nearest-neighbor Heisenberg spin glass wherein weak random anisotropy couples the chiral and spin degrees of freedom. As a result of this mixing, the CG and SG transitions occur simultaneously at $T_i \equiv T_{CG+SG}$ where the chiral Z_2 and the continuous spin-rotation SO(3) symmetries are simultaneously broken. The replica symmetry, not spontaneously broken at T_{CG+SG}, breaks at a lower temperature $T_p \equiv T_{SG}$.

VI. SUMMARY AND CONCLUSION

From the results of several attempts to synthesize the intermetallic compound Ni_5Al_3 in the nanocrystalline form by inert gas condensation technique, we conclude that, at the nanometer length scale, a stable Ni_5Al_3 compound (core) cannot be formed without a NiO shell. Detailed Rietveld refinement of the room temperature x-ray diffraction (XRD) patterns revealed the presence of a minor NiO phase concomitant with a major Ni_5Al_3 phase while the compositional analysis by the wavelength dispersion x-ray spectroscopy (WDS) yielded the composition of the samples as, S_1 : 84.98 % $Ni_{5+x}Al_{3-x}$ $(x = 0.0144)$ + 15.02 % NiO and S_2 : 79.80 % $Ni_{5-x}Al_{3+x}$ $(x = 0.0384)$ + 20.20 % NiO. The phase fractions estimated from the detailed WDS analysis are in excellent agreement with those obtained from the Rietveld refinement of the XRD patterns. High-resolution transmission electron microscopy indicated the core/shell nature of the Ni_5Al_3/NiO nanoparticles and a log-normal crystallite size distribution with the mean size $d \simeq 6$ nm. Zero-field (dc magnetic field, $H = 0$) linear (χ_1) and nonlinear (χ_n with $n = 2, 3, 4, 5$) ac-magnetic susceptibilities have been measured as functions of temperature at various ac driving field amplitudes over three decades of frequency on the nanocrystalline samples S_1 and S_2. $\chi_1(T)$ and $\chi_n(T)$ provide a conclusive evidence for the existence of two spin glass (SG) thermodynamic phase transitions: one at $T_i(H = 0) \simeq 138$ K and the other at a lower temperature $T_p(H = 0) \simeq 108$ K in both S_1 and S_2. Linear ac-susceptibility in superposed dc magnetic fields demonstrates that the thermodynamic nature of these transitions is *preserved* in finite fields and the H-T phase diagrams for the samples S_1 and S_2 are in very good agreement only with the H-T phase diagram predicted by the chirality-driven spin glass (SG) ordering model for a three-dimensional nearest-neighbor Heisenberg SG system with weak random anisotropy. A detailed comparison between theory and experiment permits us to unambiguously identify various zero-field and in-field SG phase transitions as (i) the *simultaneous* paramagnetic (PM): chiral-spin glass (CG) and PM-SG phase transitions at $T_i(H)$, and (ii) the replica symmetry-breaking SG transition at $T_p(H)$.

ACKNOWLEDGMENTS

This work is supported by the Indian National Science Academy under Grant No.: SP/SS/2013/1971. P.V.P.M. thanks the Center for Nanotechnology, University of Hyderabad, for permitting the use of the PPMS-VSM/ACMS facility for the measurement of ac magnetic response.

[1] B. I. Min, T. Oguchi, H. J. F. Jansen, and A. J. Freeman, J. Magn. Magn. Mater. **54**, 1091 (1986).
[2] N. I. Kulikov, A. V. Postnikov, G. Borstel, and J. Braun, Phys. Rev. B **59**, 6824 (1999).
[3] R. Darolia, JOM **43**, 44 (1991).
[4] F. R. de Boer, C. J. Schinkel, J. Biesterbos, and S. Proost, J. Appl. Phys. **40**, 1049 (1969).
[5] T. I. Sigfusson, N. R. Bernhoeft, and G. G. Lonzarich, J. Appl. Phys. **53**, 8207 (1982).
[6] J. C. Ho, R. C. Liang, and D. P. Dandekar, J. Appl. Phys. **59**, 1397 (1986).
[7] J. H. J. Fluitman, R. Boom, P. F. De Chatel, C. J. Schinkel, J. L. L. Tilanus, and B. R. De Vries, J. Phys.: Metal Phys. **3**, 109 (1973).
[8] H. Sasakura, K. Suzuki, and Y. Masuda, J. Phys. Soc. Jpn. **53**, 754 (1984).
[9] K. Suzuki and Y. Masuda, J. Phys. Soc. Jpn. **54**, 630 (1985).
[10] M. Yoshizawa, H. Seki, K. Ikeda, K. Okuno, M. Saito, and K. Shigematsu, J. Phys. Soc. Jpn. **61**, 3313 (1992).
[11] S. N. Kaul, J. Phys.: Condens. Matter **11**, 7597 (1999).
[12] S. N. Kaul and A. Semwal, Phys. Lett. A **254**, 101 (1999).
[13] A. Semwal and S. N. Kaul, Phys. Rev. B **60**, 12799 (1999).
[14] A. Semwal and S. N. Kaul, J. Phys.: Condens. Matter **16**, 8675 (2004).
[15] S. N. Kaul, J. Phys.: Condens. Matter **17**, 5595 (2005).
[16] P. G. Niklowitz, F. Beckers, G. G. Lonzarich, G. Knebel, B. Salce, J. Thomasson, N. Bernhoeft, D. Braithwaite, and J. Flouquet, Phys. Rev. B **72**, 024424 (2005).
[17] S. N. Kaul and A. Semwal, J. Phys.: Condens. Matter **16**, 8695 (2004).
[18] A. C. Abhyankar and S. N. Kaul, J. Phys.: Condens. Matter **20**, 445227 (2008); J. Magn. Magn. Mater. **310**, e310 (2007).
[19] A. C. Abhyankar, A. Semwal, and S. N. Kaul, J. Phys.: Condens. Matter **20**, 445228 (2008).
[20] S. N. Kaul, B. Annie D'Santhoshini, A. C. Abhyankar, L. Fernández Barquín, and P. Henry, Appl. Phys. Lett. **89**, 093119 (2006).
[21] P. K. Mukhopadhyay and S. N. Kaul, Appl. Phys. Lett. **92**, 101924 (2008).
[22] S. N. Kaul, A. Semwal, and H.-E. Schaefer, Phys. Rev. B **62**, 13892 (2000).
[23] A. C. Abhyankar and S. N. Kaul, Appl. Phys. Lett. **88**, 193125 (2006).
[24] S. N. Kaul, Phys. Status Solidi B **248**, 2276 (2011).
[25] S. N. Kaul and U. Meesala, J. Magn. Magn. Mater **401**, 539 (2016).
[26] S. R. Butler, J. E. Hanlon, and R. J. Wasilewski, J. Phys. Chem. Solids **30**, 1929 (1969).
[27] K. Enami and S. Nenno, Trans. Jpn. Inst. Met. **19**, 571 (1978).
[28] P. S. Khadkikar and K. Vedula, J. Mater. Res. **2**, 163 (1987).
[29] P. S. Khadkidar, I. E. Locci, K. Vedula, and G. M. Michal, Metall. Trans. A **24**, 83 (1993).
[30] D. Schryvers and Y. Ma, J. Alloys Compd. **221**, 227 (1995).
[31] J. S. Bowles and C. M. Wayman, Metall. Trans. **3**, 1113 (1972).
[32] R. Birringer, H. Gleiter, H. P. Klein, and P. Marquardt, Phys. Lett. A **102**, 365 (1984).

[33] H. Gleiter, Prog. Mater. Sci. **33**, 223 (1989).
[34] See Supplemental Material at http://link.aps.org/supplemental/10.1103/PhysRevMaterials.3.126003 for the structural information obtained from the Rietveld refinement.
[35] L. Motevalizadeh, Z. Heidary and M. Ebrahimizadeh Abrishami, Bull. Mater. Sci. **37**, 397 (2014).
[36] N. C. Halder and C. N. J. Wagner, Acta Cryst. **20**, 312 (1966).
[37] C. A. M. Mulder, A. J. van Duyneveldt, and J. A. Mydosh, Phys. Rev. B **23**, 1384 (1981).
[38] C. A. M. Mulder, A. J. van Duyneveldt, and J. A. Mydosh, Phys. Rev. B **25**, 515 (1982).
[39] J. L. Tholence, Physica B **108**, 1287 (1981); C. A. M. Mulder, A. J. van Duyneveldt, and J. A. Mydosh, *ibid.* **113**, 123 (1982).
[40] P. C. Hohenberg and B. I. Halperin, Rev. Mod. Phys. **49**, 435 (1977).
[41] K. Gunnarsson, P. Svedlindh, P. Nordblad, L. Lundgren, H. Aruga, and A. Ito, Phys. Rev. Lett **61**, 754 (1988).
[42] J. A. Mydosh, *Spin Glasses: An Experimental Introduction* (Taylor and Francis, London, 1993).
[43] M. Picco and F. Ritort, Phys. Rev. B **71**, 100406(R) (2005).
[44] K. Hukushima and H. Kawamura, Phys. Rev. E **61**, R1008(R) (2000).
[45] D. Imagawa and H. Kawamura, Phys. Rev. Lett. **92**, 077204 (2004).
[46] D. Imagawa and H. Kawamura, Phys. Rev. B **70**, 144412 (2004).
[47] K. Hukushima and H. Kawamura, Phys. Rev. B **72**, 144416 (2005).
[48] D. X. Viet and H. Kawamura, Phys. Rev. B **80**, 064418 (2009).
[49] S. N. Kaul and S. Srinath, J. Phys.: Condens. Matter **10**, 11067 (1998).
[50] M. Gabay and G. Toulouse, Phys. Rev. Lett. **47**, 201 (1981).
[51] J. R. L. de Almeida and D. J. Thouless, J. Phys. A: Math. Gen. **11**, 983 (1978).
[52] G. Kotliar and H. Sompolinsky, Phys. Rev. Lett. **53**, 1751 (1984).
[53] H. Kawamura, J. Phys. Soc. Jpn **79**, 011007 (2010).
[54] Y. Bitla and S. N. Kaul, Euro. Phys. Lett. **96**, 37012 (2011).
[55] M. Suzuki, Prog. Theor. Phys. **58**, 1151 (1977).
[56] K. Wada and H. Takayama, Prog. Theor. Phys. **64**, 327 (1980).
[57] S. Fujiki and S. Katsura, Prog. Theor. Phys. **65**, 1130 (1981).
[58] Y. Bitla, S. N. Kaul and L. Fernández Barquín, Phys. Rev. B **86**, 094405 (2012).